

# Characterization methods for comprehensive evaluations of shielding materials used in an MRI

Nicolas Gross-Weege,<sup>a)</sup> Thomas Dey, Pierre Gebhardt, David Schug, and Bjoern Weissler  
*Department of Physics of Molecular Imaging Systems, Institute for Experimental Molecular Imaging, RWTH Aachen University, Aachen NRW 52074, Germany*

Volkmar Schulz<sup>a)</sup>  
*Department of Physics of Molecular Imaging Systems, Institute for Experimental Molecular Imaging, RWTH Aachen University, Aachen NRW 52074, Germany*  
*Philips Research Europe, Aachen NRW 52074, Germany*

(Received 10 July 2017; revised 15 November 2017; accepted for publication 20 December 2017; published 26 February 2018)

**Purpose:** In order to integrate electronic devices into a magnetic resonance imaging (MRI) scanner, shielding of the electronics with respect to the radio frequency (RF) transmit and receive system of the MRI scanner is required. Furthermore, MRI uses time-varying low-frequency magnetic fields for spatial encoding, i.e., the gradient magnetic fields. Time-varying magnetic fields induce eddy currents in all conductive elements. The eddy currents result in opposing magnetic fields, which can cause distortions of the magnetic resonance (MR) image. As shielding of lower frequencies is not feasible in this respect, an ideal shielding element should be transparent for gradient magnetic fields while providing a high RF shielding effectiveness. Furthermore, it should offer a low susceptibility to prevent distortion of the main magnetic field of the MRI. In this work, we characterize the aforesaid shielding parameters of different shielding samples.

**Methods:** We developed a nuclear magnetic resonance (NMR) probe to measure the magnetic fields to quantify the field distortions time-resolvedly. The relative distortion was introduced as a proportionality constant relating the eddy-current-inducing field changes and the field distortions. The relative distortion was measured in the frequency range from 0 to 10 kHz for all shielding samples using the NMR probe. We characterized the shielding effectiveness of the samples in the frequency range from 1 to 150 MHz using a network analyzer. We conducted all measurements with three different materials, two carbon fiber composites and copper, each in various thicknesses.

**Results:** The relative distortion of the magnetic fields induced by the carbon fiber composites samples was at least a factor of seven lower than the copper sample. A linear dependency on the sample thickness was measured for the main field distortion, the relative distortion and the shielding effectiveness. The relative distortion was roughly independent of the gradient frequency contrary to the shielding effectiveness, highly depending on the RF frequency.

**Conclusions:** We presented a very sensitive method to characterize the distortion of the main field distortion and the gradient transparency using an NMR probe. We analyzed different shielding materials regarding the main field distortion, the gradient transparency, and the shielding effectiveness. From the tested materials, we identified a carbon fiber composite with the lowest distortion on the MRI. © 2018 The Authors. *Medical Physics* published by Wiley Periodicals, Inc. on behalf of American Association of Physicists in Medicine. [<https://doi.org/10.1002/mp.12762>]

Key words: gradient transparency, image artifacts, MRI, PET-MRI, shielding

## 1. INTRODUCTION

Magnetic resonance imaging (MRI) provides anatomic information with excellent soft tissue contrast. Additional information can be measured by integrating electronic devices in the MRI scanner, such as electrocardiographs, electroencephalographs, video cameras, up to complete single photon emission computed tomography (SPECT) or positron emission tomography (PET) systems to enable bimodal imaging. PET, for example, allows to image biological functional processes with high sensitivity. Thus, the combination of PET with MRI reveals comprehensive and complementary information and is considered to be a promising hybrid imaging modality.

The integration of electronic devices into an MRI scanner is an ambitious task because the MRI scanner is a very sensitive device with respect to electromagnetic disturbances while the electronics suffer from high static and dynamic magnetic fields. So-called zipper artifacts are often visible in MR images if active electronic devices are inserted. An example is shown in Fig. 1(a): A loose synchronization cable of the Hyperion I PET insert<sup>1</sup> resulted in the emission of spurious signals that were received by the radio frequency (RF) coil. Figure 1(b) shows the clear image with the fixed synchronization cable. Therefore, adequate shielding of the electronic devices for RF fields is required.

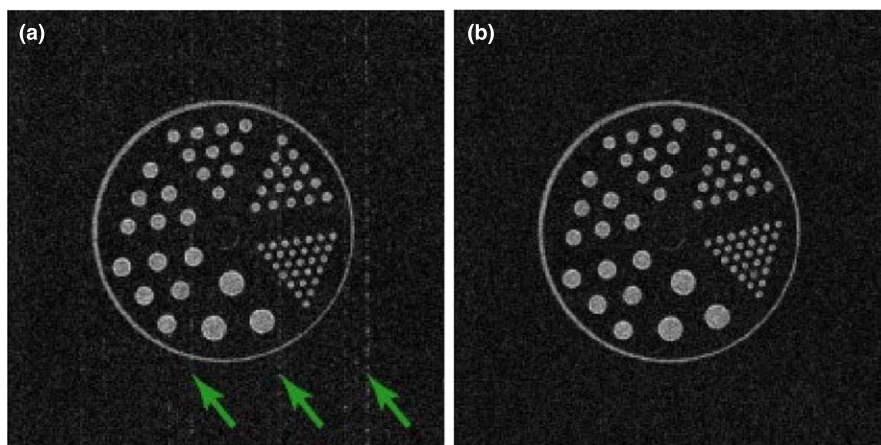


FIG. 1. Two MR images of a phantom measured with an open shielding (a) and a fixed shielding (b) of the Hyperion I<sup>1</sup> PET insert. Adapted from Ref. 2. [Color figure can be viewed at [wileyonlinelibrary.com](http://wileyonlinelibrary.com)]

A common approach is to envelope the electronics with shielding that is usually made of copper.<sup>1–5</sup> However, MRI uses fast switching gradient magnetic fields for spatial encoding. A time-varying magnetic field induces eddy currents in all conductive elements perpendicular to the changing magnetic field, such as the shieldings. The induced eddy currents flow in circular paths and decay multiexponentially.<sup>6</sup> Their strengths and decay times depend on the conductance and geometry of these elements. Reducing, e.g., the conductance and the area perpendicular to the changing field will decrease the decay times and the strength of the eddy currents. The eddy currents themselves induce superimposing magnetic fields that are opposed to the change of the gradient magnetic field. Thus, the resulting magnetic field deviates from the theoretically assumed field. As an example, Fig. 2 shows a measurement of a rectangular gradient course (30 mT/m, 200 mT/m/ms, z-direction) measured 15 cm off-center. A reference measurement is colored in blue, a measurement with a (100 × 100 × 0.1) mm copper plate placed 16 cm off-center in z-direction is colored in red. The gradient course of the measurement with the copper plate clearly differs from the reference measurement.

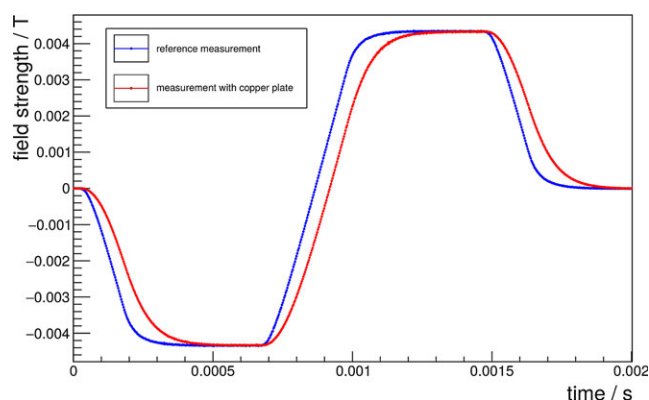


FIG. 2. Gradient course of a targeted rectangular gradient shape (30 mT/m, 200 mT/m/ms, z-direction) measured 15 cm off-center in z-direction with and without a (100 × 100 × 0.1) mm<sup>3</sup> copper plate placed 16 cm off-center in z-direction. [Color figure can be viewed at [wileyonlinelibrary.com](http://wileyonlinelibrary.com)]

Since spatial encoding in MRI relies on accurate linear gradient magnetic fields, these deviations can cause image artifacts if they are not taken into account by the image reconstruction.<sup>7–9</sup>

Thus, an ideal shielding structure should be transparent for gradient magnetic fields while providing a high RF shielding effectiveness. A high shielding effectiveness is given by a low transmittance in the RF, i.e., in the MHz range.<sup>10,11</sup> Gradient transparency can be improved by decreasing the conductance of the material in the frequency range of the gradient magnetic fields, which is typically around a few kHz. This can be done by, e.g., decreasing the conductivity of the material or the thickness of the shielding.

An additional shielding parameter of interest is a low magnetic susceptibility. High magnetic susceptibilities degrade the field homogeneity of the static magnetic field, which also leads to image distortions. Contrary to the eddy-current-induced magnetic fields, this field distortion is constant in time.

All previously mentioned shielding parameters are important for each device which is supposed to be shielded in an MRI. For PET/MRI and SPECT/MRI, one additional property of interest is a high transparency for gamma photons with an energy of a few hundreds of keV. The gamma transparency can be evaluated, e.g., by placing the shielding structure between a PET detector and a positron source and by measuring the transmitted gamma photons. Since the shielding materials are typically very thin or have a low density and proton number, their gamma transparency is very high.

In the past, different shielding approaches were investigated. In slotted shielding approaches, apertures are inserted to decrease the conductive area and hence, to decrease the strength of the eddy currents.<sup>12,13</sup> A similar approach of decreasing the conductive area are meshed structures, e.g., copper or phosphor bronze meshes.<sup>14</sup> However, gaps also lead to RF leakage and, thereby, decrease the shielding effectiveness. Carbon fibers provide a high RF shielding effectiveness, as already measured in previous works.<sup>15,16</sup> Furthermore, they are expected to be much more transparent for gradient magnetic fields than copper screens<sup>17–19</sup> and to have a low susceptibility being comparable to copper.

In summary, the desired parameters for good shielding materials are well known. However, highly sensitive and quantitative measurement methods are still lacking, especially for the gradient transparency. Common methods rely on imaging sequences, such as chemical shift imaging<sup>20</sup> or modified gradient echo sequences.<sup>17,21</sup> They do not measure the complete time course of the magnetic field and depend on the parameters of the imaging sequence. A nuclear magnetic resonance (NMR) probe can be used to measure magnetic fields time-resolvedly at a single position with high sensitivity.<sup>22,23</sup> In principle, an NMR probe can be realized as a water droplet surrounded by a transmit/receive coil.<sup>24</sup> The frequency of the NMR signal in the time domain is proportional to the magnetic field at the location of the water droplet. Thus, the complete time course of the magnetic field can be measured and no magnetic gradient fields are needed for spatial encoding.

In this work, we characterize the static field distortion, the gradient transparency and RF shielding properties of different shielding materials. We developed a NMR probe to measure and characterize the static field distortion and gradient transparency. The shielding effectiveness is characterized using a network analyzer.<sup>10</sup>

## 2. MATERIALS AND METHODS

### 2.A. NMR probe

An image of the developed NMR probe is shown in Fig. 3. We used a glass capillary with a 1.2 mm outer and 1 mm inner diameter, and a length of 25 mm. We wound a copper wire with diameter of 0.4 mm five times around the glass capillary. The latter was completely filled with water. Since the susceptibility of water (diamagnetic,  $-9.03$  ppm) highly differs from the susceptibility of air (paramagnetic,  $0.36$  ppm), we surrounded the glass capillary with an epoxy casing (diamagnetic). To increase the uniformity of the susceptibility in the epoxy casing, we suppressed the formation of air bubbles by drying the epoxy under heating in a vacuum bell.

We tuned the coil to the  $^1\text{H}$  frequency at 3 T and matched the impedance to the MRI interface. The NMR coil was connected with the coil electronics, taken from an existing one-channel Tx/Rx coil, to a clinical 3-T MRI scanner (Achieva

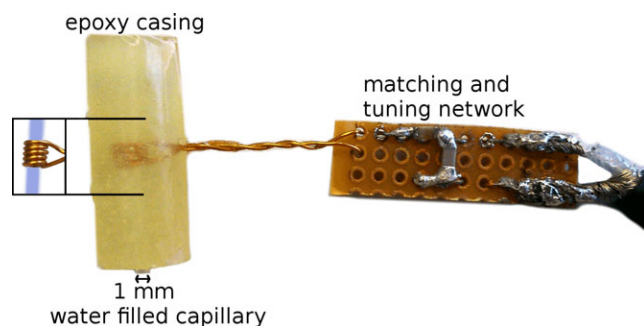


FIG. 3. Image of the developed NMR probe with epoxy casing. Capacitive impedance matching and tuning ( $^1\text{H}$  frequency at 3 T) were carried out. [Color figure can be viewed at [wileyonlinelibrary.com](http://wileyonlinelibrary.com)]

3-T, Philips, The Netherlands). The signal of the NMR probe was sampled with 91.146 kHz with the regular MRI readout electronics.

### 2.B. Data processing

The measured NMR signal in the time domain is given by the phase  $\phi$  and the magnitude. The phase points were constrained to the range from  $-\pi$  to  $\pi$ , i.e., wrapped phase. As a first step, we performed a phase unwrapping.

Furthermore, we calculated the frequency  $f$  of the signal by dividing the phase difference  $d\phi$  by the time difference  $dt$  between two points:

$$f = \frac{1}{2\pi} \frac{d\phi}{dt} \quad (1)$$

The frequency  $f$  of the NMR signal is proportional to the absolute value of the total magnetic field with the gyro magnetic ratio  $\gamma$ :

$$f = \frac{\gamma}{2\pi} \cdot \|\vec{B}\| \quad (2)$$

The time-independent magnetic field at a position  $\vec{r}$  in the field of view (FOV) of an MRI scanner is given by the main field  $\vec{B}_0$  and the main field distortion  $\Delta\vec{B}_0(\vec{r})$ . Usually, the orientation of the main field is chosen parallel to the  $z$ -axis. The main field distortion results from static effects, e.g., manufacturing tolerances of the main field coil or susceptibility variations in the FOV and can be reduced by applying shimming.<sup>25</sup> Thus, the main field distortion is spatial-dependent and also has a component perpendicular to the  $z$ -axis. Aside from tissue properties, susceptibility variations can also be caused by temperature changes.<sup>26</sup> Since the temperature changes are very low on the measurement time scale compared to the expected distortion, the effect can be neglected.

The time-dependent magnetic field at a position  $\vec{r}$  is given by the gradient field  $\vec{G}(\vec{r}, t)$  and gradient field distortion  $\Delta\vec{G}(\vec{r}, t)$ . An ideal gradient field is linear and parallel to the  $z$ -axis. The gradient field distortion results from dynamic effects, e.g., magnetic fields that are induced by eddy currents or inaccuracies of the gradient amplifiers. Thus, it is spatial- and time-dependent and can also have a component perpendicular to the  $z$ -axis.

We simplify the following calculations and consider only the  $z$ -component of the magnetic field because the other components are expected to be much smaller. In summary, the total magnetic field  $B$  at a position  $\vec{r}$  and time  $t$  can be described as:

$$B(\vec{r}, t) = B_0 + \Delta B_0(\vec{r}) + G(\vec{r}, t) + \Delta G(\vec{r}, t) \quad (3)$$

Inserting the total magnetic field, i.e., Eq. (3), in Eq. (2) yields:

$$f^{\text{total}}(\vec{r}, t) = \frac{\gamma}{2\pi} \cdot (B_0 + \Delta B_0(\vec{r}) + G(\vec{r}, t) + \Delta G(\vec{r}, t)) \quad (4)$$

Usually, the NMR signal is demodulated by the resonance frequency of the main field and  $B_0$  can be neglected. Furthermore, the main field distortion  $\Delta B_0(\vec{r})$  can be determined by

a gradient-less measurement and subtracted from the frequency data. Only time-dependent components are left:

$$f(\vec{r}, t) = \frac{\gamma}{2\pi} \cdot (G(\vec{r}, t) + \Delta G(\vec{r}, t)) \tag{5}$$

Neglecting the distortion related to the gradient coil, the magnetic field of a measurement without a sample under investigation can be associated with the undistorted gradient field  $G(\vec{r}, t)$  in Eq. (5). Calculating the difference of a measurement with a sample and without a sample at the same position yields the magnetic field distortion caused by the eddy currents in the sample:

$$f(\vec{r}, t) - \frac{\gamma}{2\pi} \cdot G(\vec{r}, t) = \frac{\gamma}{2\pi} \cdot \Delta G(\vec{r}, t) \tag{6}$$

In first order, the magnetic field distortion is proportional to the induced eddy currents in the sample, which are proportional to the time derivative of the magnetic field at the position of the sample  $\vec{r}_{sample}$  due to the law of induction:

$$\Delta G(\vec{r}, t) = -a(\vec{r}, t) \cdot \frac{dG(\vec{r}_{sample}, t)}{dt} \tag{7}$$

We introduce the constant of proportionality  $a$ , called *relative distortion*, which depends on the geometry and conductivity of the sample. It can be used to estimate the magnetic field distortion caused by eddy currents for a given input field.

### 2.C. Samples under investigation

We conducted tests with three different materials. Two carbon fiber composite materials (FuturaComposites, The Netherlands), the Fut-CRFS-11 and the Fut-CRFS-18, were compared with a copper sheet. The two carbon fiber composite materials were not characterized in previous works. All samples under investigation were  $(10 \times 10)$  cm<sup>2</sup> in size with different thicknesses.

### 2.D. Main field distortion

The NMR probe was placed 15 cm off-center and each sample were located 16 cm off-center in z-direction, as depicted in Fig. 4. The main field distortion  $\Delta B_0(\vec{r})$  was determined by a gradient-less measurement as described in Section 2.B. A reference measurement without a sample was performed to subtract the main field distortion of the MRI scanner itself.

### 2.E. Gradient transparency

The NMR probe and each sample were placed in the same way as depicted in Fig. 4 and described in Section 2.D. Additionally, a so-called chirp gradient was applied in z-direction.<sup>27,28</sup> A chirp gradient is a sinusoidal oscillation with a linear frequency increase over time. The instantaneous frequency of a chirp gradient with the duration  $T$  and the frequency range from  $f_1$  to  $f_2$  is:<sup>27</sup>

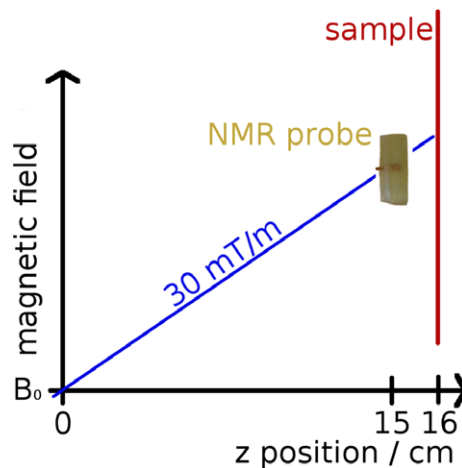


Fig. 4. Setup used for the eddy current measurements. [Color figure can be viewed at wileyonlinelibrary.com]

$$f(t) = f_1 + (f_2 - f_1)t/T \tag{8}$$

Hence, the chirp gradient waveform is given by:

$$G_C(t) = A \sin(2\pi(f_1t + (f_2 - f_1)t^2/2T)) \tag{9}$$

The amplitude  $A$  needed to be scaled down for higher frequencies because of the slew rate limit of the MRI gradient system, which was 200 mT/m/ms. For the measurements, we set the frequency range to (0–10) kHz, the strength to the maximum of 30 mT/m, the duration to 25 ms and the number of signal averages to 20. The dwell time of the gradient samples was restricted to 6.4  $\mu$ s. The chirp gradient course for the given parameters is shown in Fig. 5.

The chirp gradient applied in z-direction ensured a rapidly changing magnetic field at the sample position. We performed a measurement with chirp gradient for each sample and two additional measurements without a sample, one at the same position as the measurements with the sample, 15 cm off-center, and one at the position of the sample, 16 cm off-center. As a measure for the gradient transparency, we calculated the temporal mean value of the relative distortion for all samples, as described in Section 2.B.

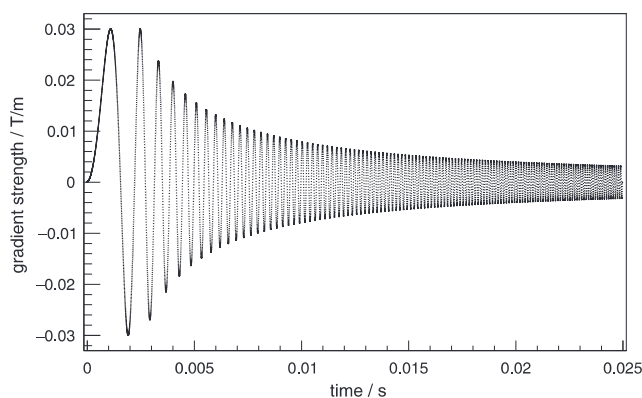


Fig. 5. Chirp gradient with a frequency range of (0–10) kHz, a duration of 25 ms and a maximum strength of 30 mT/m.

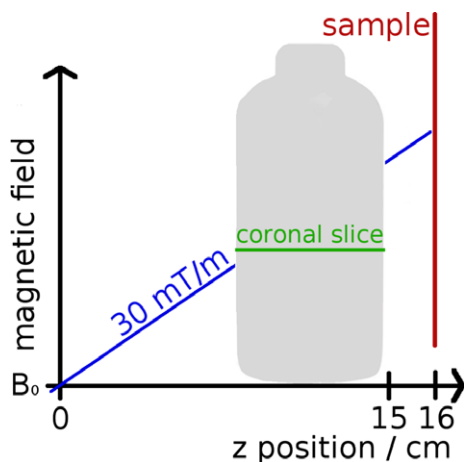


FIG. 6. Setup used to measure the influence on the MR image. [Color figure can be viewed at wileyonlinelibrary.com]

### 2.F. Shielding effectiveness

The shielding effectiveness is the ratio of the power received with and without a shielding sample for the same incident power and is given in units of decibels (dB). The shielding effectiveness of all materials was measured with a network analyzer (Agilent E5071C) and two single wound coils in the frequency range from 1 to 150 MHz (10 and 25 mm coils of the near field probe set RF2 by Langer EMV Technik, Germany). The incoming signals were amplified by a 30 dB amplifier (PA303 by Langer EMV Technik, Germany). To reduce the influence of the coupling between the two cables, the amplifier was connected directly to the receiving coil. Each sample under investigation was placed in between the two coils. Additionally, we performed a reference measurement without a sample for the normalization and a measurement with the unplugged transmit coil.

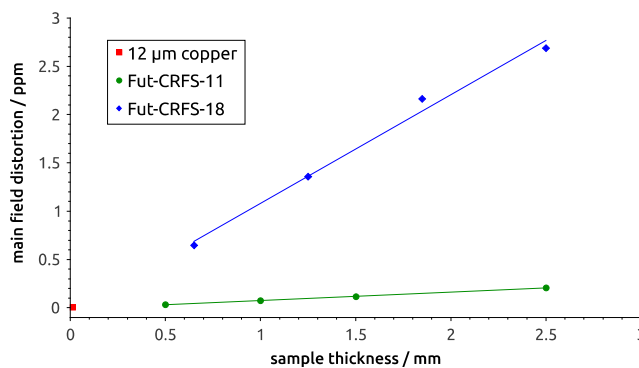


FIG. 7. Main field distortion 1 cm in front of each sample. [Color figure can be viewed at wileyonlinelibrary.com]

### 2.G. Influence on MR image

To investigate the influence of each material on the MR image, we placed a bottle phantom at the position of the NMR probe as shown in Fig. 6. A coronal slice was measured with an EPI FFE sequence with following parameters: TE/TR of 41.7/84.7 ms, EPI factor of 55, and matrix size (x,y) of (256,220). For reconstruction, the system default 2D nonlinear phase correction was applied.

## 3. RESULTS

### 3.A. Main field distortion

The measurements of the main field distortion located 1 cm in front of the sample are depicted in Fig. 7. A linear fit was applied for each carbon fiber composite material. A linear dependency of the main field distortion on the samples' thicknesses is observable. The field distortion of the 12-μm-thick copper sample was about 0 ppm. The field distortion of the Fut-CRFS-11 samples was slightly higher, i.e., lower than

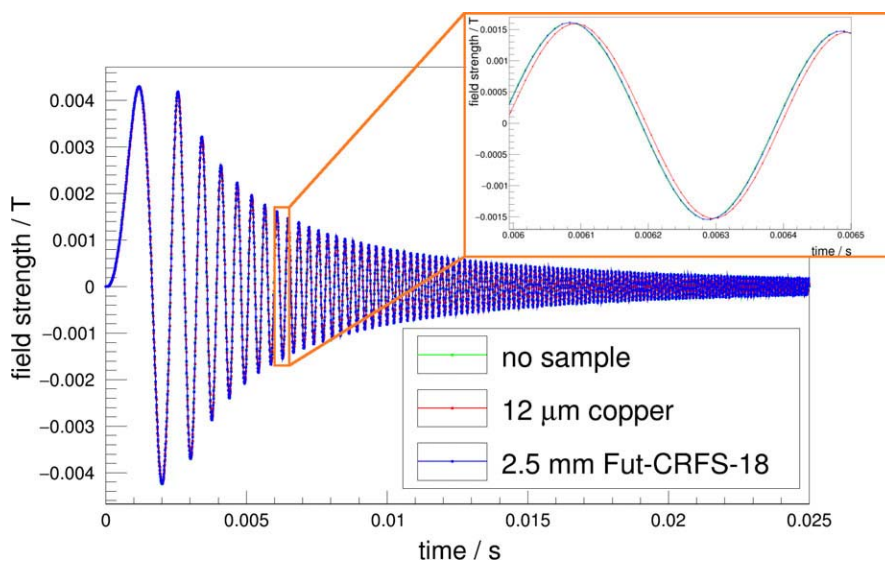


FIG. 8. The complete time course of the chirp measurements with the 12-μm-thick copper sample, the 2.5-mm-thick Fut-CRFS-18 sample, and without a sample. A zoom in the range from (0.006 to 0.0065) s is shown on the top right. [Color figure can be viewed at wileyonlinelibrary.com]

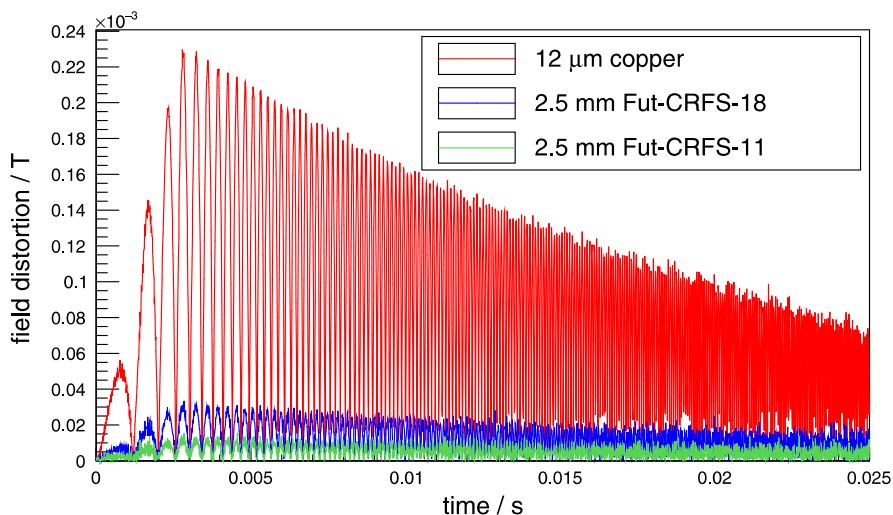


FIG. 9. Difference of the measurement with a sample and without a sample, i.e., field distortion caused by the eddy currents for the 12- $\mu$ m-thick copper sample, the 2.5-mm-thick Fut-CRFS-18 sample, and the 2.5-mm-thick Fut-CRFS-11 sample. [Color figure can be viewed at wileyonlinelibrary.com]

0.2 ppm. The Fut-CRFS-18 samples strongly disturbed the main field up to 2.7 ppm.

### 3.B. Gradient transparency

The chirp gradient measurements for the 12- $\mu$ m-thick copper sample and the 2.5-mm-thick Fut-CRFS-18 sample are shown in Fig. 8. The reference measurement without a sample was added. The frequency was calculated as a function of the magnetic field strength as shown in Eq. (2). Furthermore, a plot in the range from 6 to 6.5 ms is shown. The measurement of the 12- $\mu$ m-thick copper sample clearly differed from the reference measurement.

The difference of the measurement with and without a sample is depicted in Fig. 9. It equals the distortion caused by the sample, as calculated for Eq. (6). A strong distortion

was observable at the time points of high field changes in the chirp gradient course.

The relative distortion was calculated from Eq. (7) and is depicted in Fig. 10 for the Fut-CRFS-18 samples. The division by the time derivative of the reference measurement caused high fluctuations of the relative distortion at the time points of low field changes, i.e., low slope in the chirp gradient course. The field change was low especially at the beginning and at the maxima and minima of the chirp gradient. Neglecting the statistical fluctuations, the relative distortion was constant over time. The same behavior can also be observed for the relative distortion of the Fut-CRFS-11 samples.

The temporal mean values were calculated from Fig. 10 and are presented in Fig. 11 for all samples. We added a linear fit for each carbon fiber composite material. A linear

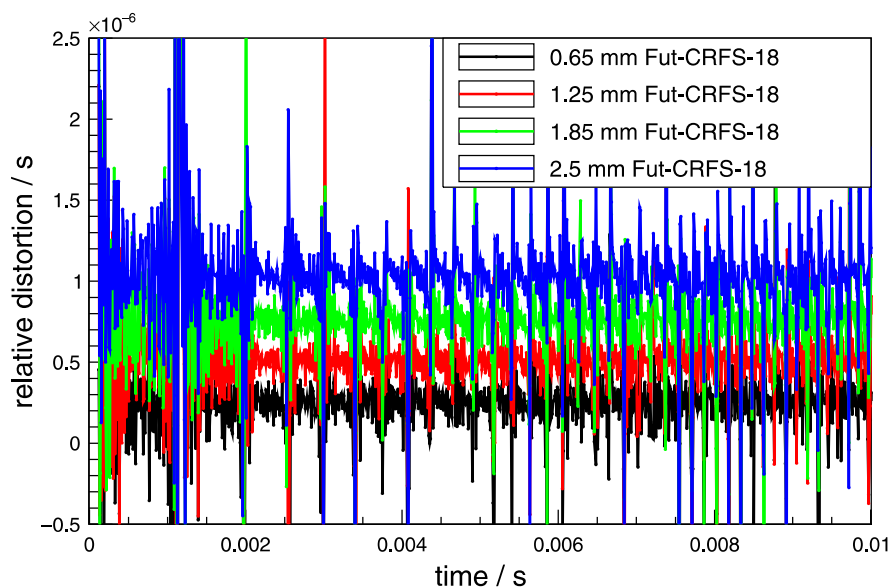


FIG. 10. Relative distortion for all Fut-CRFS-18 samples. [Color figure can be viewed at wileyonlinelibrary.com]

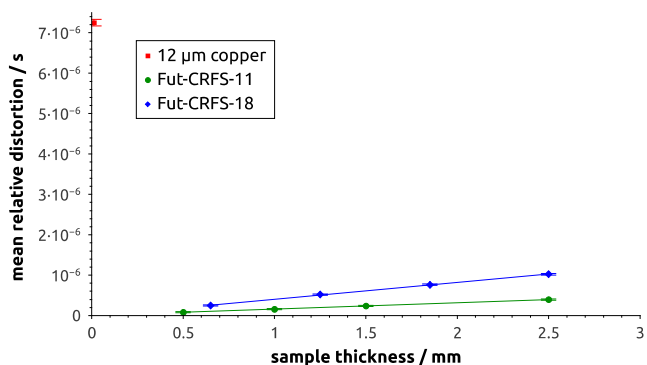


FIG. 11. Temporal mean of the relative distortion for all samples. [Color figure can be viewed at wileyonlinelibrary.com]

dependency of the relative distortion on the thickness of the sample was observable. The largest distortion was caused by the 12-μm-thick copper sample. For all carbon fiber composite samples, the relative distortions were at least a factor of seven lower than for the 12-μm-thick copper sample. The distortion caused by the Fut-CRFS-11 was a factor of about 2.6 lower than the distortion caused by the Fut-CRFS-18 of the same sample thickness.

### 3.C. Shielding effectiveness

The measurement results of the shielding effectiveness are presented in Fig. 12. The measurement without the coil showed a sensitivity limit of about 90 dB, decreasing to frequencies higher than roughly 100 MHz. The shielding effectiveness of all samples was below the sensitivity limit. Only the shielding effectiveness of the 2.5-mm-thick Fut-CRFS-18 sample reached the sensitivity limit at 100 MHz and decreased to higher frequencies similar to the measurement without the coil.

The shielding effectiveness of the 1.85-mm-thick Fut-CRFS-18 sample was on a similar level as the shielding

effectiveness of the 12-μm-thick copper sample for frequencies higher than 60 MHz. The shielding effectiveness of a Fut-CRFS-18 sample was approximately as high as the shielding effectiveness of a Fut-CRFS-11 sample of twice the thickness.

The shielding effectiveness strongly depends on the frequency. It increased for all samples to higher frequencies, except for the 2.5-mm-thick Fut-CRFS-18 which reached the sensitivity limit. The slope of the shielding effectiveness curve was steeper for the carbon fiber composite samples than for the copper sample. Therefore, the shielding effectiveness curve of the 12-μm-thick copper sample intersects the shielding effectiveness curve of the 1.85-mm- and 2.5-mm-thick Fut-CRFS-18 sample.

Figure 13 shows the shielding effectiveness versus the sample thickness at 63.9 MHz, i.e., the <sup>1</sup>H frequency at 1.5-T, including a linear fit for each carbon fiber composite material. The thickness of a sample was roughly proportional to the shielding effectiveness in decibel.

### 3.D. Influence on MR image

The MR images are depicted in Figs. 14(a)–14(d). Figure 14(a) shows the reference image without a sample. Figure 14(b) was acquired with the 12-μm-thick copper sample and ghosting artifacts were observable. The coronal cross section of the phantom in Fig. 14(c), measured with the 2.5-mm-thick Fut-CRFS-18 sample, is clinched. Fig. 14(d), measured with the 2.5-mm-thick Fut-CRFS-11 sample, looks similar to Fig. 14(a), meaning that no distortion is visible.

## 4. DISCUSSION

### 4.A. Gradient transparency

A strong distortion of the magnetic field was observable at time points of high field changes in the chirp gradient course

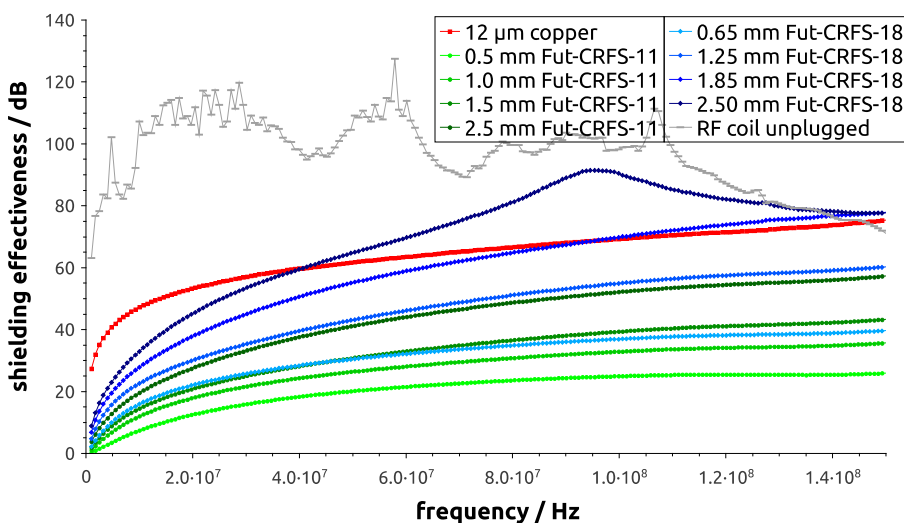


FIG. 12. Frequency-dependent shielding effectiveness for each sample. Additional measurement with the unplugged RF coil showing the sensitivity limit is colored in gray. [Color figure can be viewed at wileyonlinelibrary.com]

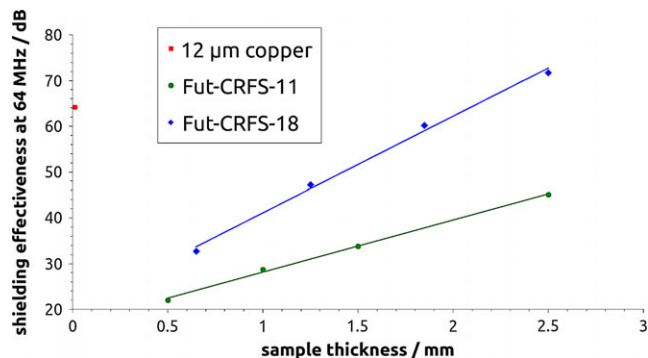


FIG. 13. Shielding effectiveness at 63.9 MHz for each sample. [Color figure can be viewed at [wileyonlinelibrary.com](http://wileyonlinelibrary.com)]

and therefore stems from the eddy currents induced in the samples. Figure 10 shows that the relative distortion was roughly constant except for the statistical fluctuation over the measurement time. The conductivity of the material was almost constant in the frequency range from 0 to 10 kHz.

The mean relative distortion of the copper sample was at least a factor of seven higher than the field distortion of all carbon fiber composite samples, which demonstrates that the conductivity of copper is much higher in the frequency range of the gradient fields. It is even more noteworthy given the fact that the carbon fiber composite samples were much thicker. Since the sample thickness is proportional to the conductance, a linear dependency on the field distortion was measured.

The relative distortion of the Fut-CRFS-18 samples was about a factor of 2.6 higher compared to the Fut-CRFS-11 samples for the same sample thickness, revealing the higher conductivity of the Fut-CRFS-18 carbon fiber composite.

With the measurement method presented in this paper, we showed a high sensitivity to magnetic field measurements and, thus, magnetic field distortions. In contrast to the established characterization with arbitrary MR imaging sequences, the method enables to measure the complete gradient time course and allowed a precise classification of the samples regarding the gradient transparency. In principle, even higher sensitivities could be reached by either improving the field homogeneity inside the NMR probe or increasing the number of signal averages.

Furthermore, the relative distortion could be measured for higher frequencies that are limited by the gradient system of

the MRI. Due to the slow rate limitation of the gradient system, the gradient strength and therefore the sensitivity of the method drops for higher frequencies.

The method could also be enhanced to measure contactlessly the conductivity of metals in the frequency range of the gradients similar to the approach of Bean et al.<sup>29</sup>

#### 4.B. Main field distortion

Since the magnetic susceptibility of copper is very low, nearly no main field distortion was observable. The same holds true for the susceptibility of the Fut-CRFS-11 samples. The Fut-CRFS-18 samples strongly disturbed the main field indicating that the Fut-CRFS-18 material comprises a magnetic component. A linear dependency of the main field distortion on the samples' thicknesses was observable because of a linear increase of the susceptibility.

#### 4.C. Shielding effectiveness

Only the shielding effectiveness of the 2.5-mm-thick Fut-CRFS-18 sample reached the sensitivity limit for frequencies higher than 100 MHz. The decrease of the shielding effectiveness for frequencies higher than 100 MHz was caused by the coupling between the two cables. The sensitivity limit can be increased by using a network analyzer with a better amplifier or a better shielding of the two cables.

The shielding effectiveness for carbon fiber composite samples decreased more rapidly to lower frequencies compared to the copper sample. Considering the results of the eddy current measurements, which state a low conductivity of the carbon fiber composite samples for frequencies in the kHz range, it indicates that the decrease of the shielding effectiveness to lower frequencies was caused by a lower conductivity.

The dependence of the thickness of a sample on the shielding effectiveness in decibel was approximately linear according to the model of White, which predicts the shielding effectiveness for composite materials.<sup>15,30</sup> The same relationship also applies for thin plane metal sheets, e.g., copper sheets, following the Schelkunoff formula.<sup>31</sup>

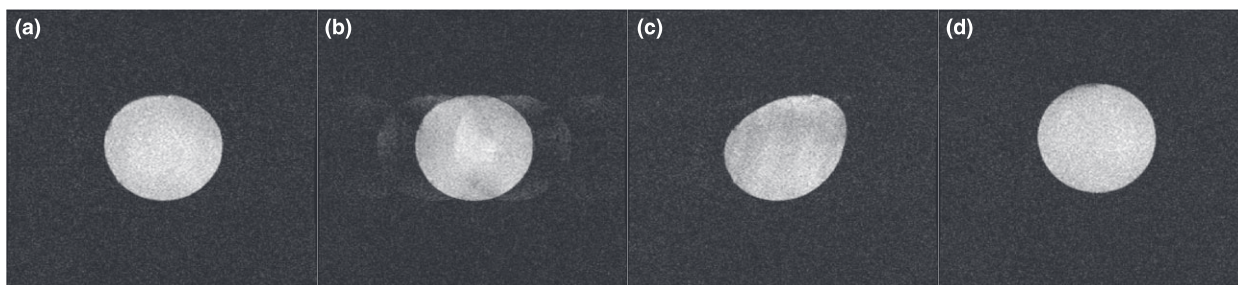


FIG. 14. MR images acquired with an EPI FFE sequence: (a) without a sample, (b) the 12-µm-thick copper sample, (c) the 2.5-mm-thick Fut-CRFS-18 sample, (d) the 2.5-mm-thick Fut-CRFS-11 sample.



#### 4.D. Influence on MR image

The quantitative results of the main field distortion and gradient transparency are clearly visible in the image. Ghosting artifacts are observable in the image acquired with the copper sheet, which were caused by the field distortion induced by the eddy currents. The image acquired with the Fut-CRFS-18 sample does not show ghosting artifact because of the high gradient transparency, but is clinched because of the high main field distortion.

A gradient-intense sequence was used that is very sensitive to magnetic field distortions. However, larger RF shields than the  $(10 \times 10)$  cm<sup>2</sup> samples are needed to shield a complete PET detector. Especially the relative distortion increases strongly with the area of the conductive material. Furthermore, positions near to the gradient coil will increase the strength of the induced eddy currents and, therefore, the distortion.

The static main field distortion depends on the distance of the FOV to the RF shield but is independent of the position of the RF shield inside the MRI. To some extent, it could be reduced by applying shimming.


#### 5. CONCLUSION AND OUTLOOK

We presented very sensitive methods to characterize the shielding parameters of different materials. We developed an NMR probe to measure and analyze the main field distortion and the gradient transparency. The shielding effectiveness was characterized using a network analyzer. Copper and the Fut-CRFS-11 showed a very low main field distortion contrary to the Fut-CRFS-18 that showed a static field distortion up to 2.7 pm 1 cm in front of the sample. The relative distortion of all carbon fiber composite samples was at least a factor of seven lower than the relative distortion of the copper sample. Thus, the Fut-CRFS-11 was the best material to minimize artifacts of the MRI. However, its shielding effectiveness of up to 45 dB at 64 MHz was lower than the shielding effectiveness of the other two materials. In following works, the required shielding effectiveness will be evaluated. Furthermore, we are working on improving the shielding effectiveness of the Fut-CRFS-11 and characterizing other materials.

#### ACKNOWLEDGMENTS

We thank FuturaComposites for the fabrication of the carbon fiber composite samples. We thank Marcel Straub for the fruitful discussions.

This research was supported by the START research program, RWTH Aachen University (innovation program of the Ministry of Science and Research NRW).

This project has received funding from the European Union's Horizon 2020 research and innovation programme under grant agreement No 667211. 

#### CONFLICTS OF INTEREST

The authors have no relevant conflicts of interest to disclose.

<sup>a)</sup>Author to whom correspondence should be addressed. Electronic mails: nicolas.gross-weege@pmi.rwth-aachen.de, schulz@pmi.rwth-aachen.de.

#### REFERENCES

- Weissler B, Gebhardt P, Lerche CW, et al. Mr compatibility aspects of a silicon photomultiplier-based pet/rf insert with integrated digitisation. *Phys Med Biol.* 2014;59:5119.
- Weissler B. Digital PET/MRI for preclinical applications. PhD thesis, Dissertation, RWTH Aachen, 2016.
- Judenhofer MS, Wehrl HF, Newport DF, et al. Simultaneous pet-mri: a new approach for functional and morphological imaging. *Nat Med.* 2008;14:459–465.
- Yoon HS, Ko GB, Kwon SI, et al. Initial results of simultaneous pet/mri experiments with an mri-compatible silicon photomultiplier pet scanner. *J Nucl Med.* 2012;53:608–614.
- Hamamura MJ, Ha S, Roeck WW, et al. Development of an mr-compatible spect system (mrspect) for simultaneous data acquisition. *Phys Med Biol.* 2010;55:1563.
- Jehenson P, Westphal M, Schuff N. Analytical method for the compensation of eddy-current effects induced by pulsed magnetic field gradients in nmr systems. *J Magn Reson (1969).* 1990; 90: 264–278.
- Ahn C, Cho Z. Analysis of the eddy-current induced artifacts and the temporal compensation in nuclear magnetic resonance imaging. *IEEE Trans Med Imaging.* 1991;10:47–52.
- Jezzard P, Barnett AS, Pierpaoli C. Characterization of and correction for eddy current artifacts in echo planar diffusion imaging. *Magn Reson Med.* 1998;39:801–812.
- Wilm BJ, Barnet C, Pavan M, Pruessmann KP. Higher order reconstruction for mri in the presence of spatiotemporal field perturbations. *Magn Reson Med.* 2011;65:1690–1701.
- Truhn D, Kiessling F, Schulz V. Optimized rf shielding techniques for simultaneous pet/mr. *Med Phys.* 2011;38:3995–4000.
- Fahy S, Kittel C, Louie SG. Electromagnetic screening by metals. *Am J Phys.* 1988;56:989–992.
- Berneking A, Trinchero R, Ha Y, et al. Design and characterization of a gradient-transparent rf copper shield for pet detector modules in hybrid mr-pet imaging. *IEEE Trans Nucl Sci.* 2017;64:1118–1127.
- Kang J, Choi Y, Hong KJ, et al. Characterization of cross-compatibility of small animal insertable pet and mri. In Nuclear Science Symposium Conference Record (NSS/MIC), 2009 IEEE, IEEE, 2009;3816–3821.
- Lee BJ, Watkins RD, Chang C-M, Levin CS. Low eddy current rf shielding enclosure designs for 3t mr applications. *Magn Reson Med.* 2017;79:1745–1752.
- Keith JM, Janda NB, King JA, Perger WF, Oxby TJ. Shielding effectiveness density theory for carbon fiber/nylon 6, 6 composites. *Polym Compos.* 2005;26:671–678.
- Heiser JA, King JA, Konell JP, Sutter LL. Shielding effectiveness of carbon-filled nylon 6, 6. *Polym Compos.* 2004;25:407–416.
- Duppenbecker PM, Wehner J, Renz W, et al. Gradient transparent rf housing for simultaneous pet/mri using carbon fiber composites. In Nuclear Science Symposium and Medical Imaging Conference (NSS/MIC), 2012 IEEE, IEEE, 2012; 3478–3480.
- Peng BJ, Wu Y, Cherry SR, Walton JH. New shielding configurations for a simultaneous pet/mri scanner at 7t. *J Magn Reson.* 2014;239:50–56.
- Weissler B, Gebhardt P, Duppenbecker PM, et al. A digital preclinical pet/mri insert and initial results. *IEEE Trans Med Imaging.* 2015;34:2258–2270.
- Peng BJ, Walton JH, Cherry SR, Willig-Onwuachi J. Studies of the interactions of an mri system with the shielding in a combined pet/mri scanner. *Phys Med Biol.* 2009;55:265.

21. Wehner J, Weissler B, Dueppenbecker P, et al. Mr-compatibility assessment of the first preclinical pet-mri insert equipped with digital silicon photomultipliers. *Phys Med Biol*. 2015;60:2231.
22. De Zanche N, Barmet C, Nordmeyer-Massner JA, Pruessmann KP. Nmr probes for measuring magnetic fields and field dynamics in mr systems. *Magn Reson Med*. 2008;60:176–186.
23. Doty FD, Entzminger G, Yang YA. Magnetism in high-resolution nmr probe design. i: general methods. *Concepts Magn Reson*. 1998;10:133–156.
24. Barmet C, De Zanche N, Wilm BJ, Pruessmann KP. A transmit/receive system for magnetic field monitoring of in vivo mri. *Magn Reson Med*. 2009;62:269–276.
25. Gruetter R, Boesch C. Fast, noniterative shimming of spatially localized signals. in vivo analysis of the magnetic field along axes. *J Magn Reson (1969)*, 1992;96:323–334.
26. Gultekin DH, Gore JC. Temperature dependence of nuclear magnetization and relaxation. *J Magn Reson*. 2005;172:133–141.
27. Addy NO, Wu HH, Nishimura DG. Simple method for mr gradient system characterization and k-space trajectory estimation. *Magn Reson Med*. 2012;68:120–129.
28. Vannesjo SJ, Dietrich BE, Pavan M, et al. Field camera measurements of gradient and shim impulse responses using frequency sweeps. *Magn Reson Med*. 2014;72:570–583.
29. Bean C, DeBlois R, Nesbitt L. Eddy-current method for measuring the resistivity of metals. *J Appl Phys*. 1959;30:1976–1980.
30. White DR, Mardiguian M. *A Handbook Series on Electromagnetic Interference and Compatibility: Electromagnetic Shielding*. Washington, DC: Interference Control Technologies, 1988.
31. Schelkunoff SA. *Electromagnetic Waves*. D. Van Nostrand, 1943.